Pressure-induced electronic anomaly and multiband superconductivity in the doped topological insulator Nb_{x}Bi_{2}Se_{3}

Mingtao Li, Kailang Xu, Ming Xu, Yifei Fang, Zhipeng Yan, Nana Li, Zhenhai Yu, Jinbo Zhang, Curtis Kenney-Benson, Xiaoli Wang, and Lin Wang

Phys. Rev. B **100**, 224521 — Published 31 December 2019

DOI: 10.1103/PhysRevB.100.224521

Pressure-induced electronic anomaly and multiband superconductivity in doped topological insulator $Nb_xBi_2Se_3$

Mingtao Li[1†], Kailang Xu[2†], Ming Xu[2†], Yifei Fang[3], Zhipeng Yan[1], Nana Li[1], Zhenhai Yu[4], Jinbo Zhang[1], Curtis Kenney-Benson[5], Xiaoli Wang,[6,*] Lin Wang[1,7*]

[1]Center for High Pressure Science and Technology Advanced Research, Shanghai 201203, China

[2]School of Optical and Electronic Information, Huazhong University of Science and Technology, Wuhan 430074, China

[3]Department of Physics, Fudan University, Shanghai 200433, China

[4]School of Physical Science and Technology, ShanghaiTech University, Shanghai, 201210, China

[5]High Pressure Collaborative Access Team, Geophysical Laboratory, Carnegie Institution of Washington, Argonne, Illinois 60439, USA

[6]School of Physics and Electronic Engineering, Linyi University, Linyi 276005, China

[7]Center for High Pressure Science (CHiPS), State Key Laboratory of Metastable Materials Science and Technology, Yanshan University, Qinhuangdao, Hebei 066004, China

†Authors contribute equally to this work.

***Corresponding Author:** linwang@ysu.edu.cn (L. W.), or wxl@lyu.edu.cn (X.L. W.)

ABSTRACT

The tunability of the electronic topological transition (ETT) is fundamentally important to unveil new quantum matters. Here, we report the observation of pressure-induced electronic anomaly below 12.0 GPa in $Nb_{0.25}Bi_2Se_3$ using a combination of electrical transport, synchrotron X-ray diffraction, Raman scattering spectroscopy measurements and first-principles calculations. At ambient pressure, the band-structure calculations demonstrate the $Nb_{0.25}Bi_2Se_3$ is a heavily electron-doped semiconductor with multiple band structure. With applying pressure, it is shown that the pressure can induce Fermi surface reconstruction at time reversal invariant point. We further present the first evidence of multiband superconductivity characterized by an upward curvature in the upper critical field in the pressurized $Nb_{0.25}Bi_2Se_3$ crystal. The superconducting critical parameters of pressurized $Nb_{0.25}Bi_2Se_3$ crystal are obtained. Furthermore, the superconducting phase diagram under high pressure is discussed within BCS theory. These new findings highlight the critical role of the

multiple-band structure induced by strong hybridization between the Nb-4d and Bi/Se-p orbitals in accessing novel quantum states.

I. INTRODUCTION

The chemical doping or pressure-induced ETT or Lifshitz transition is a change in the Fermi surface topology (FST) without symmetry breaking [1]. It is significant for discovering new quantum matters, such as nontrivial semimetal [2,3], and the enhancement and/or occurence of superconductivity [4-6]. Superconductivity may be closely related to the FST change, as reported in the quasi-2D multiband superconductor 2H-$NbSe_2$ [7].

As potential topological superconductors [8], the doped topological insulators $M_xBi_2Se_3$ (M=Cu, Nb, Sr) are currently attracting more interest due to their novel superconducting properties, i.e., the nematic superconductivity in Cu/Sr/Nb-doped [9-12], unconventional zero-bias conductance peak in Cu/Nb-doped [13-16], and vortex pinning dynamics associated with the peak effect in Cu-doped [17,18]. Despite sharing some similarities, the Nb-doped Bi_2Se_3 is distinct from the others in three main aspects [16,19,20]. Firstly, the Nb dopants strongly prefer to occupy intercalation sites for the minimized total energy compared to other Wyckoff sites [16,19]. Secondly, the Nb atoms with partially occupied $4d$-orbital states may possess magnetic moments, leading to coexistence of ferromagnetism and superconductivity [19,21]. Lastly, the occupied Nb-4d states can form new energy bands within the narrow bulk band gap [16] by hybridization with the Bi/Se-p orbital states near Fermi level (E_F), resulting in multiple Fermi surfaces [20]. However, it is tricky to synthesize fully bulk superconducting $M_xBi_2Se_3$ samples [19,22-24]. Due to intrinsic inhomogeneity, not all $M_xBi_2Se_3$ batches even from the same ingot become superconducting. The internal strain caused by dopants seems to be a crucial factor for triggering superconductivity [25]. This could somehow explain the loss of superconductivity or the significant decrease of the T_c in exfoliated thin flakes from Cu or Nb-doped Bi_2Se_3 bulk crystals [8,16].

From a band theory perspective, the $M_xBi_2Se_3$ materials are heavily doped narrow-gap semiconductors, whose electronic states are expected to be highly susceptible to external pressure. Compared with chemical doping, electric-gating, and magnetic fields, pressure is a clean and effective tool for exploring new quantum states [26], e.g., insulator-metal-superconductor transitions [27], topological quantum phase transitions [28,29], and unconventional superconductivity [30,31]. Under high pressure, the superconducting $Nb_{0.25}Bi_2Se_3$ crystal suprisingly shows a positive hydrostatic pressure dependent T_c up to 0.6 GPa [32], unlike the suppression of T_c in $Sr_{0.10}Bi_2Se_3$ up to 2.2 GPa [33] and $Cu_{0.30}Bi_{2.1}Se_3$ up to 2.31 GPa [34]. Another controvertial issue in prototype Bi_2Se_3 is whether the ETT exists as Raman scattering and theoretical calculations [35,36] and Hall effect results are inconsistent [31,37,38]. Given the unique multiband structures and layered crystal structure in Nb-doped Bi_2Se_3, it provides an tunable platform for accessing the electronic phase transition such as Lifshitz transition in Bi_2Se_3-based topological materials.

In this work, we report the pressure-induced electronic anomaly below 12.0 GPa in a non-superconducting $Nb_{0.25}Bi_2Se_3$ crystal. Above 12.0 GPa and 22.3 GPa, two first-order structural phase transitions (SPT) were also assigned. Intriguingly, we observed distinct superconducting behavior divided by the border of a monoclinic-tetragonal transition and discuss the signatures of multiband superconductivity and a semi-dome shaped $T_c(P)$ in tetragonal phase.

II. EXPERIMENTAL AND COMPUTATIONAL METHODS

A. Experimental details

The $Nb_{0.25}Bi_2Se_3$ single crystal was grown by melt method. The source materials with stoichiometric composition of high purity metals Nb (99.97%), Bi (5N) and Se (5N) lumps were loaded into an evacuated ampoule. The growth was carried out by slowly cooling the mixture from 1148 K to 900 K at a rate of 2.5 K/h in a box furnace. After growth, the crystals were annealed at 900 K for more than 24 h and then quenched into an ice water bath. We also used the same method to prepare the parent Bi_2Se_3 single crystal.

High-pressure electrical transport measurements were carried out using standard four probes method under von der Pauw configuration in a commercial DynaCool PPMS (QD) [39]. A nonmagnetic BeCu diamond anvil cell (DAC) was used to generate high pressure condition. The thin crystals were loaded into a BeCu-DAC with a diamond culet of 300 μm (sample size of ~80×70×20 μm^3 for run 1, ~60×60×10 μm^3 for run 3) and 250 μm (~70×70×20 μm^3 for run 2). Four pieces of thin platinum foil (thickness~2 μm) were utilized as the contacts in each run (see Fig. S1). Nonmagnetic BeCu alloys with a thickness of 250 μm were used as a gasket, and the pre-indented hole was covered by cubic boron nitride (C-BN) as an insulating layer. The samples were put onto a soft KBr pressure transmitting medium (PTM) with a small ruby ball sitting inside.

The high-pressure synchrotron angle-dispersive XRD of the Bi_2Se_3 and $Nb_{0.25}Bi_2Se_3$ powder was measured at 16BM-D station (photon energy 30 keV), HPCAT, Advanced Photon Source. A symmetrical Mao-Bell DAC was used to generate high pressure and mineral oil was used as PTM. The raw 2-dimenssional (2D) XRD images were integrated into 1D reflections versus two-theta angles using Dioptas [40]. The distance between the sample and detector, and its set-up parameters was calibrated using standard CeO_2. The XRD patterns were further analyzed by Retvield refinement using the GASA program package with a user interface EXPGUI [41,42].

The high-pressure Raman spectra were measured in a Raman microscope spectrometer (Renishaw, UK) with un-polarized 633 nm He-Ne laser excitation. The symmetrical Mao-Bell DAC was used to generate high pressure and mineral oil was used as the PTM. The pressure in all measurements in this work was determined from the standard ruby fluorescence [43].

B. First-principles calculations method

First-principles calculations were performed with the Vienna *ab initio* Simulation Package (VASP) [44], which is based on density functional theory (DFT). Good agreement with the experimental results was obtained using the projection plane wave pseudopotential method [45,46] and the generalized gradient approximation in the Perdew-Burke-Ernzerhof form (GGA-PBE). A unit cell of $Nb_{0.25}Bi_2Se_3$ with 21 atoms was constructed and the lattice parameters and internal atomic position of it were fully optimized until the total residual forces were smaller than 10^{-3} eV/Å to obtain a reasonably stable structure under pressure. The weak van der Waals interaction between the Bi-Se quintuple layer was taken into account by employing the DFT-D2 method of Grimme [47]. The obtained structure was then used to calculate the electronic structure including the band structure and density of state. The spin-orbit coupling (SOC) effect was introduced into the calculation of the electronic structures because it has a significant effect on the band structure of elements with an atomic number greater than 80, e.g., Bi.

III. SAMPLE SYNTHESIS AND PHYSICAL PROPERTIES AT HIGH PRESSURE

A. Crystal growth and characterization

At ambient pressure, the Nb-doped Bi_2Se_3 system crystallizes into a rhombohedral structure ($R\bar{3}m$, No. 166, CN=6) like parent Bi_2Se_3. The XRD patterns of the as-grown single crystals were collected by an x-ray diffractometer with Cu K_α radiation on a PANalytical x-ray diffractometer, as shown in Fig. 1(a). The enlarged c-axis lattice parameter in the $Nb_{0.25}Bi_2Se_3$ crystal indicates the Nb atom was intercalated into the von der Waals gap of Bi_2Se_3. The strong reflections of $(00l)$ indicates good crystallinity for the as-grown samples. As seen in Fig. 1(b), the resistivity of the $Nb_{0.25}Bi_2Se_3$ crystal shows metallic behavior and no superconductivity was observed down to 2 K. We note that the resistivity of the $Nb_{0.25}Bi_2Se_3$ crystal was smaller than the parent, which can be ascribed to its higher carrier density as indicated by the higher Hall coefficient. At ambient pressure, unlike $Cu_xBi_2Se_3$ [17,22,48], the $R_H(T)$ in $Nb_{0.25}Bi_2Se_3$ bulk crystal shows an unusual linear increase down to 20 K, implying that conductivity is involved in multi-relaxation time due to multiple bands crossing E_F [20,49]. The Nb dopants may severely modify the pristine FST to produce the considerable change in the magnitude of the Fermi velocity (v_F) [20,50].

B. Electrical transport properties at high pressure

Figure 2 (a) shows the in-plane resistance as a function of temperature, $R_{xx}(T)$, under various pressures up to 49.8 GPa. Note that the ambient data point was obtained without using DAC. Unexpectedly, unlike the metallic behavior of $R_{xx}(T)$ in bulk crystal, the thin samples show semiconducting behavior and the $R_{xx}(P)$ shows an abnormal increase below 8.7 GPa. Actually, the exfoliated thin flakes of Bi_2Se_3 show semiconducting behavior at ambient conditions [51]. The exfoliation-induced modification of the electronic band was also reported in exfoliated thin films of $Cu_xBi_2Se_3$ [52]. These results indicate the Fermi level of thin flakes of Bi_2Se_3-based materials may be different from the bulk. In $Nb_{0.25}Bi_2Se_3$ crystal, the $R_{xx}(T)$ at 0.6 GPa indeed shows semiconducting behavior (see Fig. S2 for an overview of the

$R_{\mathrm{xx}}(T)$ curves for three runs), accompanying with a considerable decrease of mobility. With the application of larger pressure, a very small resistance dip at 4.26 K was observed above 5.9 GPa (run 2, see Fig. S3 for details). In run 2, we also plotted the Hall channel data at 5.9 GPa and 8.7 GPa, in which the resistance drop is more prominent than the longitudinal resistance channel. This indicates the minority drop mainly originated from the sample center, which shall have a higher pressure than the sample edge caused by the pressure gradient. At 19.1 GPa, the magnetic field could shift the resistance drop temperature towards lower temperature and its drop percentage is also diminished, which is consistent with the features of superconductivity. Therefore, the suppression of the dip temperature and reduction of the resistance drop supports the origin of superconductivity. At 30.4 GPa and above, the resistance dropped sharply to zero, suggesting a bulk superconducting state was achieved. The pressure induced resistance change and zero resistance transition can be reproduced in run 3, suggesting the observed electrical transport phenomena is intrinsic.

The Hall effect was measured to explore the underlying changes in the electronic structure. The Hall resistance (R_{xy}) versus the applied field (B) at 20 K shows linear field dependence with negative slopes indicative of dominant electron-type (n-type) carriers, as shown in Fig. 2 (b) and (c). We note the $R_{\mathrm{H}}(P)$ and $\mu_{\mathrm{H}}(P)$ results are reproducible in run 3 (see Fig. 3). The symmetrized $R_{\mathrm{xy}}(B)$ was obtained by the difference of the Hall resistance at positive and negative fields to eliminate the longitudinal contribution, i.e., $R_{\mathrm{xy}}(B) = \left[R_{\mathrm{xy}}(+B) - R_{\mathrm{xy}}(-B)\right]/2$. The Hall mobility μ_{H} was determined by $\mu_{\mathrm{H}} = (d/\rho_{\mathrm{xx}})R_{\mathrm{xy}}/B$ [39], where d is the sample thickness. We plotted the R_{H} and Hall mobility (μ_{H}) as a function of pressure in Fig. 2(c). For comparison, the values of the Hall coefficient and mobility at 300 K (20 K) under the ambient pressure are extracted to be -0.58 (-0.53) cm^{-3}/C and 3383.5 (4450.1) cm^{2}/V s. At 20 (300) K, an unusual decrease in $R_{\mathrm{H}}(P)$ was observed with a minimum reached at 5.9 (8.7) GPa, above which it increases quickly and attains saturation when $P > 30.4$ GPa. This feature is strikingly different from Bi_2Se_3 [31,37,38]. A slight decrease of n was also reported in $Cu_{0.30}Bi_{2.1}Se_3$ up to 2.31 GPa [34]. Meanwhile, the $\mu_\mathrm{H}(P)$ below 11.8 GPa shows a V-shape character with a valley at 8.7 GPa, above which a dramatic increase occurs, signaling abrupt changes of the FST. Hence, the electronic anomalies in $Nb_{0.25}Bi_2Se_3$ are likely attributed to the pressure-induced modification of the electronic band topology.

From $R_\mathrm{H}(T)$ and $\mu_\mathrm{H}(T)$ under different pressure (see Fig. S4), we observed the temperature or pressure-induced sign change in R_H [53], indicating a significant reconstruction of the Fermi surface. For instance, at 28.5 GPa and 36.4 GPa, a $p-n$ transition was observed at 300 K, as seen in Fig. 3(a)-(b). Importantly, the pressure dependence of $R_\mathrm{H}(P)$ and $\mu_\mathrm{H}(P)$ at 300 K and 20 K was reproducible in run 3 (see Fig. 3(c)), verifying the pressure-induced electronic anomalies in $Nb_{0.25}Bi_2Se_3$. Figure 4(a) shows a typical $R(T)$ curve at 7.6 GPa (run 3) in R-phase. With decreasing temperature, the resistance increases dramatically and a resistance hump characterized by the dR/dT change appears at around 80.4 K. Other two resistance anomalies were observed at 6.7 K and 250 K, as indicated in inset of Fig. 4(a). Coexistence of p-type and n-type carriers is demonstrated by the non-linear $R_\mathrm{xy}(B)$ at 7.6 GPa, as seen in Fig. 4(b). This suggests the n-type and p-type carriers may give a synergetic contribution to the complicated conductivity by different scattering times at high pressure, supporting the existence of multiple Fermi surface in the R-phase for $Nb_{0.25}Bi_2Se_3$. All the results point to the multiple band structure in the R-phase and high-pressure phase for $Nb_{0.25}Bi_2Se_3$ [20,50].

C. Superconducting properties at high pressure

To investigate magnetic field effects on superconductivity, we measured the suppression of superconductivity by external fields. Fig. 5(a)-(b) shows plotted representatives at 30.4 GPa and 49.8 GPa, and Fig. 5(c)-(d) shows the upper critical field with temperature, $B_\mathrm{c2}(T)$. Besides the shift of the T_c, the suppression of the superconducting transition is not always parallel but can be divided into two parallel sectors by a critical field. This striking feature characterized by an upward curvature (or kink), is clearly displayed in the $B_{\mathrm{c2}}(T)$ or normalized $b^*(t)$ curves in Fig. 5(c) and (d). This is unusual compared to Bi_2Se_3 [31], $Cu_{0.30}Bi_{2.1}Se_3$ [34], and $Sr_{0.19}Bi_2Se_3$ [54], in which quasilinear $B_{\mathrm{c2}}(T)$ was observed. The kink of $B_{\mathrm{c2}}(T)$ may reveal multiband superconductivity, as demonstrated in other layered superconductors, e.g., $NbSe_2$ [55], MgB_2 [56], and FeSe [57]. As shown in Fig. 3 and Fig. S4, the slope changes in $R_{\mathrm{xy}}(B)$ from positive to negative either below 300 K or above 28.5 GPa at 300 K (run 3), signaling a temperature- or pressure-driven $p-n$ transition. This proves the multiband feature in $Nb_{0.25}Bi_2Se_3$ under high pressure, leading to our conjecture that the kink originates from multiband superconductivity.

To calculate $B_{\mathrm{c2}}(T)$ at 0 K, we simply fitted the $B_{\mathrm{c2}}(T)$ by the modified Ginzburg-Landau (GL) relation, $B_{\mathrm{c2}}^{\mathrm{GL}}(T) = B_{\mathrm{c2}}^{\mathrm{GL}}(0)[(1-t^2)/(1+t^2)]^m$, where m is a constant. Interestingly, all $B_{\mathrm{c2}}(T)$ data can be well fitted, and the yielded parameters are plotted in the inset of Fig. 5(c). The large $B_{\mathrm{c2}}(0)$ suggests type-II superconductivity. Using a weak coupling relation $\kappa = 3.54 \times 10^4 (\rho_0 |\, dB_{\mathrm{c2}}/dT \,|_{T_{\mathrm{c}}})^{1/2}$ and $B_{\mathrm{c}}(0) = (T_{\mathrm{c}} |dB_{\mathrm{c2}}/dT|_{T_{\mathrm{c}}})/2.45\kappa$ in dirty limit [58], the GL parameter κ and thermal dynamical critical $B_{\mathrm{c}}(0)$ were estimated to be 31.5 and 34.5 mT at 30.4 GPa, indicating that it is a strong type-II superconductor. The lower critical field can thus be calculated by $B_{\mathrm{c1}}(0) = B_{\mathrm{c}}(0)\ln\kappa/(\sqrt{2}\kappa)$, yielding 2.7 mT at 30.4 GPa. Due to the difficulty of implementing such high pressure to heat capacity measurements, we indirectly estimated the electronic coefficient and density of states (DOS) at E_{F} with the relation $\gamma_{\mathrm{s}} = B_{\mathrm{c}}^2(0)/2\pi T_{\mathrm{c}}^2 = \frac{1}{3}\pi^2 k_{\mathrm{B}}^2 N(E_{\mathrm{F}})$ [59], which yields 1.81 mJ/mol K^2 and $N(E_{\mathrm{F}})$=2.02 states/eV-atoms $spin^{-1}$ per formula unit (f. u.) at 30.4 GPa, larger than ambient $Cu_{0.29}Bi_2Se_3$ [48]. This indicates the pressurized $Nb_{0.25}Bi_2Se_3$ metallized. If adopting the orbital-limited Werthamer-Helfand-Hohenberg (WHH) formula with a dirty limit [60], $B_{\mathrm{c2}}^{\mathrm{orb}}(0) = -0.693 T_{\mathrm{c}} dB_{\mathrm{c2}}/dT|_{T_{\mathrm{c}}}$, this will yield much smaller $B_{\mathrm{c2}}^{\mathrm{orb}}(0)$ than the GL fitted value (see Table I). On the other hand, the values of $b^*(t)$ at 0 K below 49.8 GPa are considerably larger than the expected $b_{\mathrm{WHH}}^*(0) \cong 0.693$ for orbital-limited [60] or $b^*_{\mathrm{pp}}(0)$ ≅0.85 for polar p-wave superconductivity [61]. Table I summarizes the derived superconducting critical parameters, in which the $B_{\mathrm{c1}}(0)$, $B_{\mathrm{c}}(0)$, γ_{s}, and $N(E_{\mathrm{F}})$ values set the upper-bound for the band with the largest energy gap.

To get more qualitative insights into the superconducting properties, we adopted the relation $S = -\left(dB^{\mathrm{orb}}_{\mathrm{c2}}/dT\right)\big|_{T_{\mathrm{c}}}/T_{\mathrm{c}} \propto 1/\nu^2_{\mathrm{F}}$, for a single-band superconductor [53,62], where ν_{F} is Fermi velocity determining the slope of the energy dispersion $E(k)$ at the Fermi level. Since the difference in the slope is $dB^{\mathrm{orb}}_{\mathrm{c2}}/dT$, we extracted the slopes above (S_{a}) and below (S_{b}) the kink temperature by linear fitting to represent the two respective bands in good approximation. The T_{c} of the latter was defined as an intercept to the temperature axis at 0 T. More strict treatment definitely needs the individual ν_{F} values determined by quantum oscillations within a two-band model [62]. We plot the $-\left(dB^{\mathrm{orb}}_{\mathrm{c2}}/dT\right)\big|_{T_{\mathrm{c}}}/T_{\mathrm{c}}$ as a function of pressure in the inset of Fig. 5(d). The S_{a} firstly increases at a small rate but shows a larger increasing rate above 35.8 GPa, whilst a slight decrease between 35.8 and 42.8 GPa for S_{b}, which seems involve a significant Fermi surface change. Above 42.8 GPa, both S_{a} and S_{b} show a nearly parallel increase. Altogether, the single-band WHH and polar p-wave models are inadequate for interpreting the observed $B_{\mathrm{c2}}(T)$ data in pressurized $Nb_{0.25}Bi_2Se_3$.

D. Normal state properties at ambient and high pressure

In pure metals, the resistivity behaves with decreasing temperature as $\rho \propto T^5$ below the Debye temperature (Θ, Θ_{D}: obtained from specific heat, Θ_{R}: obtained from electrical resistivity) while $\rho \propto T$ for $T > \Theta$ [63]. However, in materials with anisotropic Fermi surfaces, the electrons are from different orbital state bands. Thus, scatterings of electrons from either intra-states or inter-states will contribute to conductivity. In the electron-phonon (e-p) scattering Umklapp-processes (U-process), an exponential factor $\rho \propto \exp(-\theta/T)$ is expected to appear in resistivity. Therefore, the normal state resistivity versus temperature in $Nb_{0.25}Bi_2Se_3$ can be tentatively written with the following relation [63]

$$\rho(T) = \rho_0 + A \cdot T^2 + B \cdot \exp(-\theta/T), \text{(1)}$$

where the ρ_0 is the residual resistivity from impurity scattering, the second term represents the contribution of electron-electron (e-e) scattering, and the last one relates to the e-p scattering of the U-process. For U-process e-p scattering, the crystal momentum is written as $\boldsymbol{k} + \boldsymbol{q} = \boldsymbol{k}' - \boldsymbol{g}$, where $\boldsymbol{k}$ and $\boldsymbol{k}'$ are electron wave vector before and after scattering, $\boldsymbol{q}$ phonon wave vector, $\boldsymbol{g}$ an non-zero arbitrary vector of the reciprocal lattice resulting in the change of the electron wave vector ($\boldsymbol{g}$ =0 corresponds to normal-process, N-process). We note that the fitting parameter θ in Eq. (1) is related to the Debye temperature by $\theta = \Theta/\beta$ with $\beta = Q/q_0$ (Q Debye radius, q_0 the shortest distance between the Fermi surface and its image). We found that the experimental data of both the ambient R-phase and T-phase in bulk Bi_2Se_3 and $Nb_{0.25}Bi_2Se_3$ can be well fitted by Eq. (1), as shown in Fig. 6. At low temperature, the ρ(T) curve was dominated by the first two terms, indicating the dominant electron-electron interaction. At higher temperature, the U-process e-p scattering contributes more to resistivity.

The specific heat measurements indicates the Θ_D is between 140-200 K for bulk Bi_2Se_3 [64], ~120 K for bulk $Cu_{0.29}Bi_2Se_3$ [48]. By fitting the ρ(T) curve using Eq. (1), we obtained θ=164.67 K and θ=128.07 K for Bi_2Se_3 and $Cu_{0.20}Bi_2Se_3$ with T_c=3.54 K [18], respectively. Therefore, $\theta \cong \Theta_D \cong \Theta_R$ ($\beta \cong$1) applies to bulk Bi_2Se_3 and $Cu_{0.29}Bi_2Se_3$ at ambient pressure. We should recall here the magnitude of θ is directly proportional to the size of Θ_D with a factor of $1/\beta$, to get which one would need to know the lattice spectrum and shape of the Fermi surface et al. [63]. Here, we simply assume the β is independent of pressure and $\beta \cong$1 to track the pressure dependence of Θ_D in $Nb_{0.25}Bi_2Se_3$. One can estimate the Debye temperature by fitting ρ(T) according to Eq. (1). Since the coefficient $A \propto (m^*)^2$ [65], m^* electron effective mass, the m^* is expected to decrease as the A decreases with pressure. Furthermore, the electron-phonon coupling parameters λ could be calculated by the McMillan formula in strong-coupling [66], $\lambda = \frac{1.04 + \mu^* \ln(\Theta_D/1.45T_c)}{(1 - 0.62\mu^*)\ln(\Theta_D/1.45T_c) - 1.04}$, using μ^*=0.13. The fitted and calculated parameters are summarized in Table II. The increase of the θ in $Nb_{0.25}Bi_2Se_3$ reflects the lattice becomes stiffer as expected in a compressed solid. To our surprise, the θ also shows a dramatic increase between 35.8 and 42.8 GPa, in consistent with the behavior of S_a. Due to the electrons can be strongly scattered by transverse phonons in U-process [63], this implies the transverse phonons might play key role in the superconducting behavior in compressed tetragonal $Nb_{0.25}Bi_2Se_3$, which needs further study of the issue.

IV. STRUCTURAL EVALUATIONS AT HIGH PRESSURE

To better understand the pressure-induced superconductivity, a series of XRD patterns were measured. We observed two SPTs occurring at 12.0 GPa and 22.3 GPa. Like Bi_2Se_3 [67], the high-pressure phases are identified as monoclinic (space group: $C2/m$, No.12, CN=7) and tetragonal (space group: $I4/mmm$, No.139, CN=8) phase. Using the GASA program package with a user interface EXPGUI [41,42], we refined the XRD patterns for $Nb_{0.25}Bi_2Se_3$ and representative Rietveld refinement profiles at P=0.7 GPa, P=18.4 GPa, and P=47.1 GPa were plotted in Fig. 7(a)-(c). This means the sequence of SPTs was not affected by Nb doping. Hereafter, we denote the rhombohedral, monoclinic, and tetragonal phases as the R-phase, M-phase and T-phase, respectively. A series of XRD patterns, the refined lattice parameters and the volume V/Z *versus* pressure are plotted in Fig. 8(b) and (d). Due to dominant covalent bonding in Bi-Se quintuple layers (QPLs) and only very weak covalent bonding between QPLs spaced by von der Waals gap [68,69], this makes the expected larger compressibility of c-axis than the ab plane featured as a fast decrease of the c/a ratio. Interestingly, the ratio of c/a undergoes an abrupt drop between 4.9 and 5.4 GPa, as indicated by the dash square in Fig. 8(c). Above around 9.7 GPa, the c/a ratio rapidly rises again. This is contrast with the pressure dependence of c/a in Bi_2Se_3 [35,70].

To compare the compressibility with R-phase, we plotted the lattice parameters and the V/Z versus pressure for the M-phase and T-phase in Fig. 8(c) and (d). The $P-V/Z$ data was fitted using the third-order Birch-Murnaghan equation of state

(BM-EoS), $P = 3K_0 f_\mathrm{E}(1+2f_\mathrm{E})^{5/2} \cdot \left[1 + \frac{3}{2}(K_0' - 4)f_\mathrm{E}\right]$, where $f_\mathrm{E} = \left[(V_0/V)^{2/3} - 1\right]/2$ is the Eulerian strain, K_0 is the bulk modulus, and K_0' is the pressure derivative of K_0, V_0 the volume at ambient pressure. The best fitting yielded K_0^r=45.3(7.6) GPa, $K_0^{\prime,r}$=7.4(1.8) and V_0^r=143.1(9) Å^3 for the R-phase; K_0^m=50.1(8.3) GPa, $K_0^{\prime,m}$=4(fixed) and V_0^m=140.5(3.8) Å^3 for the M-phase; K_0^t=86.2(4.1) GPa, $K_0^{\prime,t}$=4(fixed) and V_0^t=125.1(1.0) Å^3 for T-phase. The volume collapse at the two SPTs is estimated to be 3.7% and 2.8%, indicating a first-order transition. Details of the BM-EoS fitting results comparing with other reports can be found in Table S-I.

In layered materials, the minimum of c/a is commonly attributed to the ETT [28,35], nevertheless there is a lack of smoking-gun evidence in $\mathrm{Bi_2Se_3}$-based materials at least [35,36,67]. At ambient pressure, the bottom conduction band (CB) and top valence band (VB) in $\mathrm{Bi_2Se_3}$ are dominated by the Bi-6p_z^+ and Se1-4p_z^- orbitals states with band inversion at Brillouin center [69]. After Nb doping, the partially occupied Nb-4d orbital states can form new energy bands by hybridizing with the Bi/Se-p orbital states near E_F [16,19,20]. For this reason, the electronic band structure of Nb-doped $\mathrm{Bi_2Se_3}$ is expected to be more sensitive to pressure. The drastic drop and approached minimum of c/a thus prefigure changes of chemical bonding, i.e., variations of the enhancing and/or diminishing bond length and angle. These fine structure changes might correlate to the electronic anomalies in R-phase. In fact, the bonding length and bonding angle extracted from GSAS refinement displays a significant opposite pressure dependent behavior [53], further supporting the different pressure responses between rhombohedral $\mathrm{Bi_2Se_3}$ and $\mathrm{Nb_{0.25}Bi_2Se_3}$.

V. LATTICE DYNAMICS

To further confirm the SPTs by XRD measurements, we carried out unpolarized Raman scattering spectroscopy measurements of the $\mathrm{Nb_{0.25}Bi_2Se_3}$ crystal to investigate the lattice dynamics under high pressure. The pressure dependence of selected Raman spectrum and shifts ($\omega(P)$) is shown in Fig. 9(a) and (b). In R-phase, the Nb, Bi, Se1 and Se2 locate in Wyckoff sites of $3b$, $6c$, $3a$, and $6c$ with Se1 as the inversion center, respectively. According to the group theory analysis [71,72], a total of 15 lattice dynamical modes at Γ point (q=0) are classified into 3 acoustic modes composed of one $A_{2\mathrm{u}}$ mode and a twofold-degenerated E_u modes and 12 optical modes with irreducible representations expressed by $\Gamma = 2A_{1\mathrm{g}} + 2A_{2\mathrm{u}} + 2E_\mathrm{g} + 2E_\mathrm{u}$, in which E symmetry modes are twofold-degenerated. This indicates there are four Raman-active modes ($2A_{1\mathrm{g}} + 2E_\mathrm{g}$) with even-parity and four Infrared-active modes ($2A_{2\mathrm{u}} + 2E_\mathrm{u}$) with odd-parity. As seen in Fig. 9(a), three of the Raman modes were clearly assigned. Due to the smallest phonon frequency of E_g^1 mode is out of the detection limit for present Raman spectrometer (50-9000 cm^{-1}) [73], it is not addressed in this study. Bottom insets sketch the corresponding atomic vibration for $A_{1\mathrm{g}}^1$, E_g^2, and $A_{1\mathrm{g}}^2$ modes, among which the $A_{1\mathrm{g}}$ and E_g modes denote the out-of-plane and in-plane phonon vibrations. In further, the E_g^1 and $A_{1\mathrm{g}}^1$ modes are characterized by the in-phase vibrating for Bi-Se2 pairs while opposite-phase for E_g^2 and $A_{1\mathrm{g}}^2$ modes.

Interestingly, unlike Bi_2Se_3, we observed the slope changes at around 5.84 GPa and 10.12 GPa of the three Raman modes in the R-phase for $Nb_{0.25}Bi_2Se_3$, respectively. This is indicated by the solid lines in Fig. 9(b). The relatively smaller pressure coefficient above 10.12 GPa indicates the phonon frequency abnormally softens. To uncover the pressure-induced electronic anomaly in the R-phase [74], we plotted in Fig. 9(c) the full width at half maximum (FWHM) versus pressure. Surprisingly, the FWHM of the three phonon modes shows a very contrasting evolution with pressure, i.e., both the E_g^1 and $A_{1\mathrm{g}}^1$ modes undergo a minimum at around 4.9 GPa. By contrast, the minimum occurs at around 8.2 GPa for the stretching $A_{1\mathrm{g}}^2$ mode. These unusual transitions agree with the structural anomalies assigned by XRD, supporting the intrinsic nature of the subtle pressure-induced structural changes. For comparison, the pressure coefficient of the FWHM changes only occur at around 5.0 GPa in Bi_2Se_3 [35], 4.0 GPa in Bi_2Te_3 [75], and 3.5 GPa in Sb_2Te_3 [76].

Above 12.5 GPa, new types of phonon frequencies occur, signifying an SPT from the R-phase to M-phase. According to XRD results, the structure of the high-pressure M-phase is monoclinic with space group $C2/m$ (No. 12, CN=7, formula number Z=4) [70], and all Bi1, Bi2, Se1, Se2, and Se3 atoms occupy the $4i$ Wyckoff sites. The group theory analysis predicts 30 zone-center lattice vibration modes, which can be written in an irreducible representation as $\Gamma = 10B_{\mathrm{u}} + 5A_{\mathrm{u}} + 5B_{\mathrm{g}} + 10A_{\mathrm{g}}$. There are three acoustic modes composed of one A_{u} and two B_{u} modes. The remaining 27 are optical modes including 15 Raman-active modes expressed by $\Gamma_{15}^{\mathrm{R}} = 5B_{\mathrm{g}} + 10A_{\mathrm{g}}$ and 12 Infrared-active modes $\Gamma_{12}^{\mathrm{IR}} = 8B_{\mathrm{u}} + 4A_{\mathrm{u}}$. Except the four lowest phonon frequencies with symmetry of B_{g}^{1}, A_{g}^{1}, B_{g}^{2}, and A_{g}^{2}, all the Raman-active modes were observed with a clear blueshift at high pressure above 12.5 GPa. We note that the B_{g}^{2} phonon mode may be masked by the close position and higher intensity of A_{g}^{6} and A_{g}^{7}, similar to the case in Bi_2Se_3 [35]. With further increasing pressure, the Raman peaks broadened and weakened. Eventually, all the phonon frequencies disappeared above 33.4 GPa, indicating the second M-T SPT had completed and metallization of T-phase.

VI. FIRST-PRINCIPLES CALCULATIONS

To gain deeper insights into the pressure-induced electronic anomalies in the R-phase, we performed first principles calculations of the electronic band structure. At ambient condition, the most prominent character after Nb intercalation into Bi_2Se_3 is the appearance of new energy bands with at least three bands (denoted as the α-band, β-band, and γ-band) crossing E_{F}, resulting in a heavily electron-doped semiconductor. As seen in Fig. 10, three more energy bands appear after Nb doping and the valence band close to E_{F} mainly comes from the Se-P_{x} states at ambient pressure, in contrast to the parent Bi_2Se_3 [69]. Simultaneously, the direct band gap not only became smaller ($E_{\mathrm{g}}^{\mathrm{d}}$~0.25 eV) than the parent ($E_{\mathrm{g}}^{\mathrm{d}}$~0.31 eV), but the E_{F} also crosses three conduction bands. For the Nb $4d$ electrons, the d_{z^2} and d_{xz} orbital states seem to be dominant around E_{F} (see Fig. S9 for details).

The calculated band structures up to 10.4 GPa are plotted in Fig. 11 (a)-(f). We note the CBs close to E_F have contributions from the Bi-6p, Se-4p, and Nb-4d orbital states, manifesting the significance of the orbital hybridization between the Nb and Bi/Se atoms. Under pressure up to 1 GPa, the CB tends to lift towards E_F, while a new band inversion between the α-band and β-band occurred at the G point. Meanwhile, a hole-like pocket at the L point from the γ-band disappeared at 0.30 GPa (see Fig. 12(a)). Above 4.8 GPa, the α-band lifted above E_F, indicating the disappearance of one electron-like pocket at the G point. With further increasing pressure, the β-band moved down and eventually shifted below E_F at the L point under 9.4 GPa. These results indicate the pressure can theoretically induce the Fermi surface reconstruction in multiband $Nb_{0.25}Bi_2Se_3$. Interestingly, the two minimums of the c/a ratio at around 3 GPa and 6 GPa are correlated with the valley and peak of the direct energy gap between the δ-band and VB at the G point (see Fig. 12(b)). Thus, our results emphasize the key role of the multiband structure originating from orbital hybridization between the d and p electrons in accessing the pressure-induced electronic anomaly in $Nb_{0.25}Bi_2Se_3$.

VII. DISCUSSIONS

Figure 13(a) summarized the $R_\mathrm{xx}(P)$ and $\mu_\mathrm{H}(P)$ at 300 K and 20 K. We note the electronic anomaly at much lower pressure in run 1 were probably attributed to the Bi-Se layers slide during compression [53]. Here we only focus on the run 2 and run 3 for further discussions. Below 2.2 GPa, we observed a gradual increase of R_xx and nearly stabilized μ_H. However, the R_xx tends to increase much faster above 2.2 GPa and reaches a maximum at around 7.6 GPa, above which the $R_\mathrm{xx}(P)$ not only suddenly drops but $R_\mathrm{xx}(T)$ also becomes metallic. Since XRD and Raman results ruled out the occurrence of SPTs below 12.0 GPa, the drastic change in electrical properties at around 7.6 GPa intrinsically signifies the pressure-induced changes in FST. Above 12 GPa, the peak value of Hall mobility starts to decrease gradually. However, it tends to decline rapidly above 22.9 GPa and reaches a small value of 1.45 cm^2/V s at 35.8 GPa, indicating the metallization of $Nb_{0.25}Bi_2Se_3$. To further examine the electronic anomaly in R-phase, we derived the pressure dependence of carrier density as plotted in Fig. 13(b). The results of $n(P)$ obtained with a finer pressure step shows there is an apparent decrease at around 6.4 GPa and an abrupt increase at around 7.6 GPa, as seen in inset of Fig. 13(b). We found the pressure value for $n(P)$ is slightly different from the values determined from XRD and Raman results. This is probably originating from the different pressure gradient generated by PTM. According to the report of Zhao et al [77], the KBr PTM becomes non-hydrostatic above 3-5 GPa. In our case, the rough estimation indicates the axial pressure is ~1.4 GPa higher than radial pressure at 7.6 GPa [53]. If one takes into this account, the observed anomalies in $n(P)$ can be approximately in consistent with the results of XRD and Raman scattering measurements. Moreover, the behavior of $n(P)$ in $Nb_{0.25}Bi_2Se_3$ is strikingly different from Bi_2Se_3 [31,37,38], in which it shows a monotonic increase up to 8 GPa in R-phase.

As shown in Fig. 13(b), unlike the maximized $T_c(P)$ in the M-phase for $Sr_{0.19}Bi_2Se_3$ [54] and stabilized $T_c(P)$ in the T-phase for Bi_2Se_3 [31], the T_c in $Nb_{0.25}Bi_2Se_3$ reached a maximum at around 30 GPa, and then declines at a small rate $dT_c/dP \cong$-0.079(5) K/GPa and nearly stabilizes above 42.8 GPa. Very recently, a similar $T_c(P)$ phase diagram was reported in Bi_2Te_2Se and $Bi_{1.1}Sb_{0.9}Te_2S$ [78]. On one hand, we note that the zero-resistance transition is not observed in M-phase in present experiments, which is different from the superconducting transition in Bi_2Se_3 [31,38], in Bi_2Te_2Se and $Bi_{1.1}Sb_{0.9}Te_2S$ [78], and $Sr_{0.19}Bi_2Se_3$ [54]. Although the underlying reason is not clear, we think this behavior is caused by either low carrier density or magnetic pair-breaking effect by Nb ions [53]. On the other hand, a similar saturation of the T_c with pressure was also observed in other layered systems such as metallized MoS_2 up to megabar pressure [27], which is proposed to be a characteristic of band overlap in layered materials with almost 2D $N(E_F)$ as it is independent of n. This scenario is partly true in our case based on two points. The Fermi velocity v_F^a shows a fast decrease with pressure but it is much slower above 42.8 GPa, implying the associated band structure tends to become more narrowing, an indication of becoming a quasi-2D FS. This is also in consistent with the saturation trend of R_H and μ_H above 42.8 GPa. On the other hand, the c/a ratio in the

T-phase shows an abnormal increase with pressure (see Fig. S6), also hinting at the tendency of the approach to a more 2D-layered structure upon compression.

Finally, we discuss the nature of the superconducting state in T-phase. As seen in Fig. 13(b), the n shows a gradual increase below 42.8 GPa with a saturation trend above this pressure. According to BCS theory [79], the T_c is given by $T_c = 1.14\Theta_D \exp[-1/N(E_F)V_0]$ for a phonon-mediated superconductor in a weak coupling limit, with $N(E_F) \propto m^* n^{1/3}$ and V_0 electron-electron interaction potential obeying the relation $N(E_F)V_0 = \lambda - \mu^*$. In $Cu_{0.30}Bi_{2.1}Se_3$, the suppression of the T_c by pressure was attributed to the decrease of n [34]. Apparently, the suppression of the T_c in T-phase cannot be simply ascribed to the decrease of n. By fitting $R_{xx}(T)$, we could evaluate the change of Θ_D with pressure, i.e., increasing from 119.67 K at 30.4 GPa to 147.64 K at 49.8 GPa. This means a concurrent decrease of λ was required to rebalance the T_c. Using McMillan's relation [66], the λ was calculated to decline from 1.21 at 30.4 GPa to 0.97 at 49.8 GPa, indicating strong coupling superconductivity. In the case of strong coupling, the pressure dependence of the T_c can be estimated by $d\ln T_c/d\ln V = (K_0/T_c)dT_c/dP \cong [\gamma_G + \Delta \cdot (d\ln\eta/d\ln V + 2\gamma_G)]$ [31,66,80], where $\gamma_G = -d\ln\langle\omega\rangle/d\ln V$ is Grüneisen parameter, $\Delta = 1.04\lambda(1+0.38\mu^*)/[\lambda - \mu^*(1+0.62\lambda)]^2$, and $\eta = N(E_F) < I^2 >$ the Hopfield parameter ($< I^2 >$ is an electron-ion matrix element) [81]. Using the bulk modulus K_0=86.2 GPa by XRD, dT_c/dP~0.079(5) K/GPa (30.4 GPa<P<42.8 GPa), we obtained $d\ln T_c/d\ln V = (K_0/T_c)dT_c/dP$=0.86. Since $d\ln\eta/d\ln V$ ≈-1 for s-electron or p-electron metals whilst -3~-4 for d-electron metals [80,81], we assume an intermediate coefficient -2.5 when considering the Nb-4d electrons and λ=1.08 (averaged value) herein. This yields a Grüneisen parameter of γ_G=1.16 for $Nb_{0.25}Bi_2Se_3$, slightly larger than Bi_2Se_3 (γ_G=1) [31], inferring the importance of hybridization between the Nb-4d and Bi/Se-p electrons states. Nevertheless, this value is somewhat lower than transition metals (γ_G~2 for Nb) [81] and MgB_2 (γ_G=2.36) [80].

VIII. CONCLUSIONS

In summary, we reported on the study of the pressure-induced electronic anomaly below 12.0 GPa in the rhombohedral phase and superconductivity in high pressure phase of $Nb_xBi_2Se_3$. According to the first-principles calculations, the emerging multibands at the E_F from hybridizing the Nb-4d and Bi/Se-p orbital states are critical for our findings. Two first-order SPTs were also assigned above 12.0 GPa and 22.3 GPa. Intriguingly, the monoclinic phase underwent filamentary superconductivity, while there were signatures of bulk superconductivity with a semi-dome shaped $T_c(P)$ in the tetragonal phase. We demonstrate the first evidence of multiband superconductivity in pressurized $Nb_{0.25}Bi_2Se_3$, which may be ascribed to multiple Fermi surfaces associated with Nb-4d orbital states. To fully understand the multiband superconductivity in the tetragonal phase, the precise sites of the Nb atoms must be probed experimentally by local sensitive techniques. The superconducting $Nb_xBi_2Se_3$ crystals under pressure will be investigated in the future.

ACKNOWLEDGEMENTS

We thank Hongliang Dong for the Cu_K_α target XRD measurements. This work was mainly supported by Natural Science Foundation of China (Grant No. 11874076, No. 11804011), National Science Associated Funding (NSAF, Grant No. U1530402), and Science Challenging Program (Grant No. TZ2016001). X.W. was supported by the National Natural Science Foundation of China No.s 11974154 and 11147007 and the Natural Science Foundation of Shandong Province under grant No.s JQ201602, 2019GGX103023 and ZR2018MA038. Use of the Advanced Photon Source, an Office of Science User Facility operated for the US DOE Office of Science by Argonne National Laboratory, was supported by the US DOE under Contract No. DE-AC02-06CH11357.

References

[1] I. M. Lifshitz, Sov. Phys. JETP **11**, 6 (1960).

[2] Y. Wu, N. H. Jo, M. Ochi, L. Huang, D. Mou, S. L. Bud’ko, P. C. Canfield, N. Trivedi, R. Arita, and A. Kaminski, Phys. Rev. Lett. **115**, 166602 (2015).

[3] Z. J. Xiang, G. J. Ye, C. Shang, B. Lei, N. Z. Wang, K. S. Yang, D. Y. Liu, F. B. Meng, X. G. Luo, L. J. Zou, Z. Sun, Y. Zhang, and X. H. Chen, Phys. Rev. Lett. **115**, 186403 (2015).

[4] C. Liu, T. Kondo, R. M. Fernandes, A. D. Palczewski, E. D. Mun, N. Ni, A. N. Thaler, A. Bostwick, E. Rotenberg, J. Schmalian, S. L. Bud’ko, P. C. Canfield, and

A. Kaminski, Nat. Phys. **6**, 419 (2010).

[5] M. Ren, Y. Yan, X. Niu, R. Tao, D. Hu, R. Peng, B. Xie, J. Zhao, T. Zhang, and D. L. Feng, Sci. Adv. **3**, e1603238 (2017).

[6] D. Kang, Y. Zhou, W. Yi, C. Yang, J. Guo, Y. Shi, S. Zhang, Z. Wang, C. Zhang, S. Jiang, A. Li, K. Yang, Q. Wu, G. Zhang, L. Sun, and Z. Zhao, Nat. Commun. **6**, 7804 (2015).

[7] T. Yokoya, T. Kiss, A. Chainani, S. Shin, M. Nohara, and H. Takagi, Science **294**, 2518 (2001).

[8] M. Sato and Y. Ando, Rep. Prog. Phys. **80**, 076501 (2017).

[9] K. Matano, M. Kriener, K. Segawa, Y. Ando, and G.-q. Zheng, Nat. Phys. **12**, 852 (2016).

[10] S. Yonezawa, K. Tajiri, S. Nakata, Y. Nagai, Z. Wang, K. Segawa, Y. Ando, and Y. Maeno, Nat. Phys. **13**, 123 (2016).

[11] K. Willa, R. Willa, K. W. Song, G. D. Gu, J. A. Schneeloch, R. Zhong, A. E. Koshelev, W.-K. Kwok, and U. Welp, Phys. Rev. B **98**, 184509 (2018).

[12] T. Asaba, B. J. Lawson, C. Tinsman, L. Chen, P. Corbae, G. Li, Y. Qiu, Y. S. Hor, L. Fu, and L. Li, Phys. Rev. X **7**, 011009 (2017).

[13] S. Sasaki, M. Kriener, K. Segawa, K. Yada, Y. Tanaka, M. Sato, and Y. Ando, Phys. Rev. Lett. **107**, 217001 (2011).

[14] R. Tao, Y.-J. Yan, X. Liu, Z.-W. Wang, Y. Ando, Q.-H. Wang, T. Zhang, and D.-L. Feng, Phys. Rev. X **8**, 041024 (2018).

[15] A. Sirohi, S. Das, P. Neha, K. S. Jat, S. Patnaik, and G. Sheet, Physical Review B **98**, 094523 (2018).

[16] C. Kurter, A. D. K. Finck, E. D. Huemiller, J. Medvedeva, A. Weis, J. M. Atkinson, Y. Qiu, L. Shen, S. H. Lee, T. Vojta, P. Ghaemi, Y. S. Hor, and D. J. Van Harlingen, Nano Lett. **19**, 38 (2019).

[17] M. T. Li, Y. F. Fang, Z. Sun, J. C. Zhang, and C. T. Lin, J. Phys.: Condens. Matter **30**, 31LT01 (2018).

[18] M. T. Li, Y. F. Fang, J. C. Zhang, H. M. Yi, X. J. Zhou, and C. T. Lin, J. Phys.: Condens. Matter **30**, 125702 (2018).

[19] Y. Qiu, K. N. Sanders, J. Dai, J. E. Medvedeva, W. Wu, P. Ghaemi, T. Vojta and Y. S. Hor, arXiv: 1512.03519 (2015). https://arxiv.org/abs/1512.03519

[20] B. J. Lawson, P. Corbae, G. Li, F. Yu, T. Asaba, C. Tinsman, Y. Qiu, J. E. Medvedeva, Y. S. Hor, and L. Li, Phys. Rev. B **94**, 041114(R) (2016).

[21] N. F. Q. Yuan, W.-Y. He, and K. T. Law, Phys. Rev. B **95**, 201109(R) (2017).

[22] Y. S. Hor, A. J. Williams, J. G. Checkelsky, P. Roushan, J. Seo, Q. Xu, H. W. Zandbergen, A. Yazdani, N. P. Ong, and R. J. Cava, Phys. Rev. Lett. **104**, 057001 (2010).

[23] Z. Liu, X. Yao, J. Shao, M. Zuo, L. Pi, S. Tan, C. Zhang, and Y. Zhang, J. Am. Chem. Soc. **137**, 10512 (2015).

[24] B. J. Lawson, PhD thesis, University of Michigan, (2017). http://hdl.handle.net/2027.42/140942

[25] A. Ribak, K. B. Chashka, E. Lahoud, M. Naamneh, S. Rinott, Y. Ein-Eli, N. C. Plumb, M. Shi, E. Rienks, and A. Kanigel, Phys. Rev. B **93**, 064505 (2016).

[26] H.-K. Mao, X.-J. Chen, Y. Ding, B. Li, and L. Wang, Rev. Mod. Phys. **90**, 015007 (2018).

[27] Z. Chi, X. Chen, F. Yen, F. Peng, Y. Zhou, J. Zhu, Y. Zhang, X. Liu, C. Lin, S. Chu, Y. Li, J. Zhao, T. Kagayama, Y. Ma, and Z. Yang, Phys. Rev. Lett. **120**, 037002 (2018).

[28] X. Xi, C. Ma, Z. Liu, Z. Chen, W. Ku, H. Berger, C. Martin, D. B. Tanner, and G. L. Carr, Phys. Rev. Lett. **111**, 155701 (2013).

[29] A. Bera, K. Pal, D. V. Muthu, S. Sen, P. Guptasarma, U. V. Waghmare, and A. K. Sood, Phys. Rev. Lett. **110**, 107401 (2013).

[30] J. L. Zhang, S. J. Zhang, H. M. Weng, W. Zhang, L. X. Yang, Q. Q. Liu, S. M. Feng, X. C. Wang, R. C. Yu, L. Z. Cao, L. Wang, W. G. Yang, H. Z. Liu, W. Y. Zhao, S. C. Zhang, X. Dai, Z. Fang, and C. Q. Jin, Proc. Natl. Acad. Sci. USA **108**, 24 (2011).

[31] K. Kirshenbaum, P. S. Syers, A. P. Hope, N. P. Butch, J. R. Jeffries, S. T. Weir, J. J. Hamlin, M. B. Maple, Y. K. Vohra, and J. Paglione, Phys. Rev. Lett. **111**, 087001 (2013).

[32] M. P. Smylie, K. Willa, K. Ryan, H. Claus, W. K. Kwok, Y. Qiu, Y. S. Hor, and U. Welp, Physica C **543**, 58 (2017).

[33] A. M. Nikitin, Y. Pan, Y. K. Huang, T. Naka, and A. de Visser, Phys. Rev. B **94**, 144516 (2016).

[34] T. V. Bay, T. Naka, Y. K. Huang, H. Luigjes, M. S. Golden, and A. de Visser, Phys. Rev. Lett. **108**, 057001 (2012).

[35] R. Vilaplana, D. Santamaría-Pérez, O. Gomis, F. J. Manjón, J. González, A. Segura, A. Muñoz, P. Rodríguez-Hernández, E. Pérez-González, V. Marín-Borrás, V. Muñoz-Sanjose, C. Drasar, and V. Kucek, Phy. Rev. B **84**, 184110 (2011).

[36] A. Bera, K. Pal, D. V. Muthu, U. V. Waghmare, and A. K. Sood, J. Phys.: Condens. Matter **28**, 105401 (2016).

[37] J. J. Hamlin, J. R. Jeffries, N. P. Butch, P. Syers, D. A. Zocco, S. T. Weir, Y. K. Vohra, J. Paglione, and M. B. Maple, J. Phys.: Condens. Matter **24**, 035602 (2012).

[38] P. P. Kong, J. L. Zhang, S. J. Zhang, J. Zhu, Q. Q. Liu, R. C. Yu, Z. Fang, C. Q. Jin, W. G. Yang, X. H. Yu, J. L. Zhu, and Y. S. Zhao, J. Phys.: Condens. Matter **25**, 362204 (2013).

[39] L. J. v. d. Pauw, Philips Res. Rep. **13**, 1 (1958).

[40] C. Prescher and V. B. Prakapenka, High Pressure Res. **35**, 223 (2015).

[41] A. C. L. a. R. B. V. Dreele, General Structure Analysis System (GSAS), Los Alamos National Laboratory Report LAUR 86-748 (2004).

[42] B. Toby, J. Appl. Cryst. **34**, 210 (2001).

[43] H. K. Mao, J. Xu, and P. M. Bell, J. Geophys. Res. **91**, 4673 (1986).

[44] G. Kresse and J. Furthmüller, Comput. Mater. Sci. **6**, 15 (1996).

[45] G. Kresse and D. Joubert, Phys. Rev. B **59**, 1758 (1999).

[46] P. E. Blochl, Phys. Rev. B **50**, 17953 (1994).

[47] S. Grimme, J. Comput. Chem. **27**, 1787 (2006).

[48] M. Kriener, K. Segawa, Z. Ren, S. Sasaki, and Y. Ando, Phys. Rev. Lett. **106**, 127004 (2011).

[49] A. J. S. Machado, N. P. Baptista, B. S. de Lima, N. Chaia, T. W. Grant, L. E.

Corrêa, S. T. Renosto, A. C. Scaramussa, R. F. Jardim, M. S. Torikachvili, J. A. Aguiar, O. C. Cigarroa, L. T. F. Eleno, and Z. Fisk, Phys. Rev. B **95**, 144505 (2017).

[50] B. J. Lawson, Y. S. Hor, and L. Li, Phys. Rev. Lett. **109**, 226406 (2012).

[51] O. Chiatti, C. Riha, D. Lawrenz, M. Busch, S. Dusari, J. Sanchez-Barriga, A. Mogilatenko, L. V. Yashina, S. Valencia, A. A. Unal, O. Rader, and S. F. Fischer, Sci Rep **6**, 27483 (2016).

[52] J. A. Alexander-Webber, J. Huang, J. Beilsten-Edmands, P. Cermak, C. Drasar, R. J. Nicholas, and A. I. Coldea, J. Phys.: Condens. Matter **30**, 155302 (2018).

[53] See supplementary materials for details.

[54] Y. Zhou, X. Chen, R. Zhang, J. Shao, X. Wang, C. An, Y. Zhou, C. Park, W. Tong, L. Pi, Z. Yang, C. Zhang, and Y. Zhang, Phys. Rev. B **93**, 144514 (2016).

[55] H. Suderow, V. G. Tissen, J. P. Brison, J. L. Martinez, and S. Vieira, Phys. Rev. Lett. **95**, 117006 (2005).

[56] Y. Eltsev, S. Lee, K. Nakao, N. Chikumoto, S. Tajima, N. Koshizuka, and M. Murakami, Phys. Rev. B **65**, 140501(R) (2002).

[57] U. S. Kaluarachchi, V. Taufour, A. E. Böhmer, M. A. Tanatar, S. L. Bud'ko, V. G. Kogan, R. Prozorov, and P. C. Canfield, Phys. Rev. B **93**, 064503 (2016).

[58] P. H. Kes and C. C. Tsuei, Phys. Rev. B **28**, 5126 (1983).

[59] R. Meservey and B. B. Schwartz, in Superconductivity, edited by R. D. Parks, (Marcel Dekker, New York, 1969), Vol. 1, Chap. 3, p.168.

[60] N. R. Werthamer, E. Helfand, and P. C. Hohenberg, Phys. Rev. **147**, 295 (1966).

[61] K. Scharnberg and R. A. Klemm, Phys. Rev. B **22**, 5233 (1980).

[62] V. G. Kogan and R. Prozorov, Rep. Prog. Phys. **75**, 114502 (2012).

[63] J. M. Ziman, in Electrons and Phonons: The Theory of Transport Phenomena in Solids, Oxford University Press, (1960), p369.

[64] G. E. Shoemake, J. A. Rayne, and R. W. Ure, Phys. Rev. **185**, 1046 (1969).

[65] D. Jaccard, H. Wilhelm, K. Alami-Yadri, and E. Vargoz, Physica B **259-261**, 1 (1999).

[66] W. L. McMillan, Phys. Rev. **167**, 331 (1968).

[67] Z. Yu, L. Wang, Q. Hu, J. Zhao, S. Yan, K. Yang, S. Sinogeikin, G. Gu, and H. K. Mao, Sci Rep **5**, 15939 (2015).

[68] P. Larson, Phys. Rev. B **74**, 205113 (2006).

[69] H. Zhang, C.-X. Liu, X.-L. Qi, X. Dai, Z. Fang, and S.-C. Zhang, Nat. Phys. **5**, 438 (2009).

[70] J. Zhao, H. Liu, L. Ehm, D. Dong, Z. Chen, and G. Gu, J. Phys.: Condens. Matter **25**, 125602 (2013).

[71] H. Köhler and C. R. Becker, Physica Status Solidi (b) **61**, 533 (1974).

[72] W. Richter and C. R. Becker, Physica Status Solidi (b) **84**, 619 (1977).

[73] Y. Zhao, X. Luo, J. Zhang, J. Wu, X. Bai, M. Wang, J. Jia, H. Peng, Z. Liu, S. Y. Quek, and Q. Xiong, Phys. Rev. B **90**, 245428 (2014).

[74] K. Saha, K. Legare, and I. Garate, Phys. Rev. Lett. **115**, 176405 (2015).

[75] R. Vilaplana, O. Gomis, F. J. Manjón, A. Segura, E. Pérez-González, P. Rodríguez-Hernández, A. Muñoz, J. González, V. Marín-Borrás, V. Muñoz-Sanjosé, C. Drasar, and V. Kucek, Phys. Rev. B **84**, 184110 (2011).

[76] O. Gomis, R. Vilaplana, F. J. Manjón, P. Rodríguez-Hernández, E. Pérez-González, A. Muñoz, V. Kucek, and C. Drasar, Phys. Rev. B **84**, 174305 (2011).

[77] J. Zhao and N. L. Ross, J. Phys.: Condens. Matter **27**, 185402 (2015).

[78] S. Cai, S. K. Kushwaha, J. Guo, V. A. Sidorov, C. Le, Y. Zhou, H. Wang, G. Lin, X. Li, Y. Li, K. Yang, A. Li, Q. Wu, J. Hu, R. J. Cava, and L. Sun, Phys. Rev. Mater. **2**, 114203 (2018).

[79] J. Bardeen, L. N. Cooper, and J. R. Schrieffer, Phys. Rev. **108**, 1175 (1957).

[80] T. Tomita, J. J. Hamlin, J. S. Schilling, D. G. Hinks, and J. D. Jorgensen, Phys. Rev. B **64**, 092505 (2001).

[81] J. J. Hopfield, Physica **55**, 41 (1971).

Figures

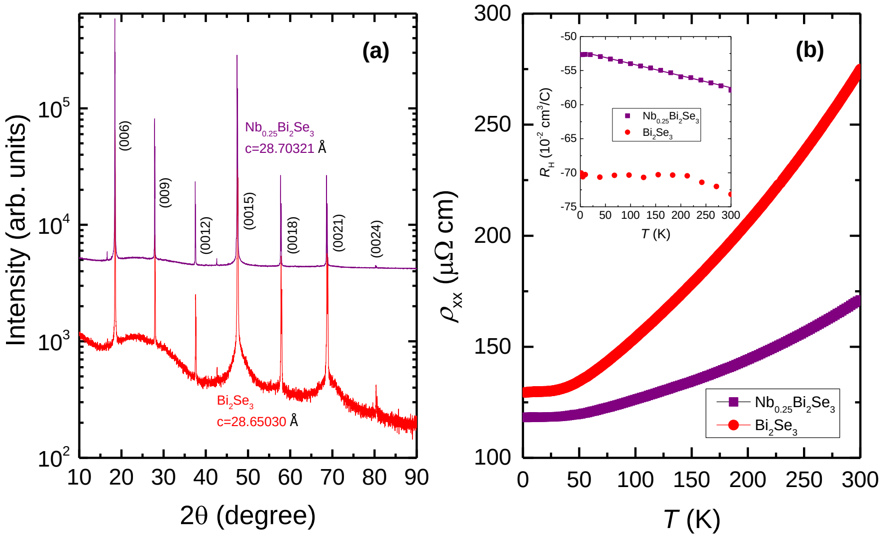

FIG. 1 (a) The single-crystal XRD patterns. (b) The temperature dependence of the bulk Bi_2Se_3 and $Nb_{0.25}Bi_2Se_3$ crystal resistivity. Inset shows the temperature dependence of Hall coefficient, and the solid line is the linear fit result as a guide to eyes for $Nb_{0.25}Bi_2Se_3$.

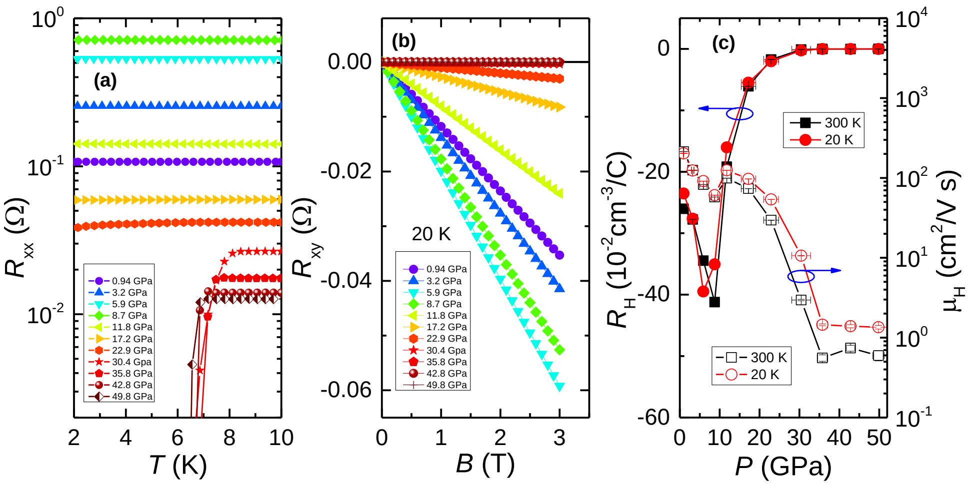

FIG. 2 (a) The $R_{xx}(T)$ under various pressures below 10 K. (b) The $R_{xy}(B)$ under various pressures at 20 K. (c) The $R_H(P)$ and $\mu_H(P)$ at 300 K and 20 K. The data was collected in run 2.

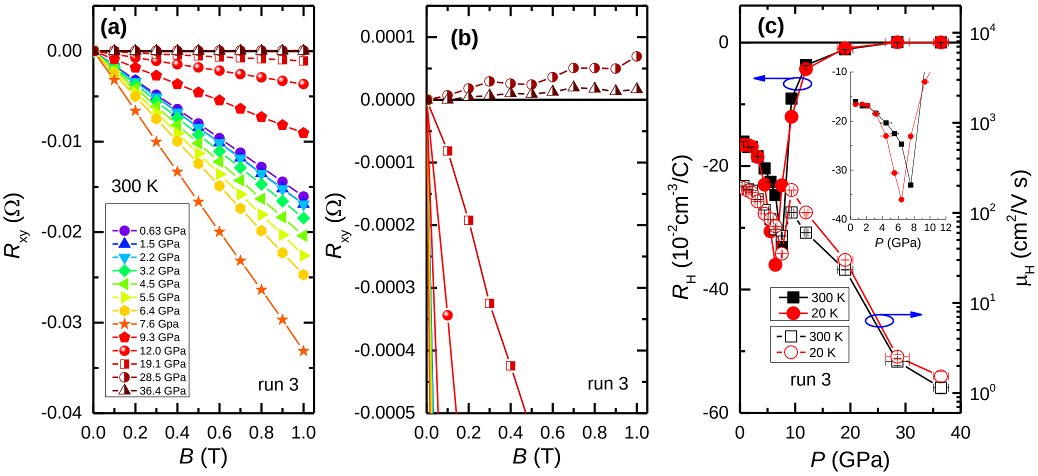

FIG. 3 (a) The Hall resistance as a function of field at 300 K for different pressures (run 3). (b) The enlarged view shows the positive slope of $R_{xy}(B)$ at 28.5 GPa and 36.4 GPa. (c) The pressure dependence of Hall coefficient and mobility at 300 K and 20 K. The inset is an enlarged view in the range of 0-12.0 GPa.

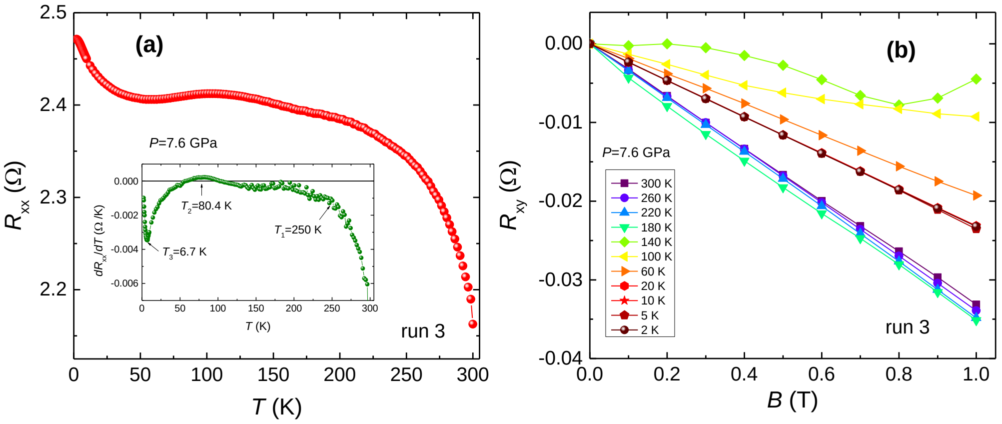

FIG. 4 (a) The resistance as a function of temperature. The inset shows its first order derivative. (b) The field dependence of Hall resistance.

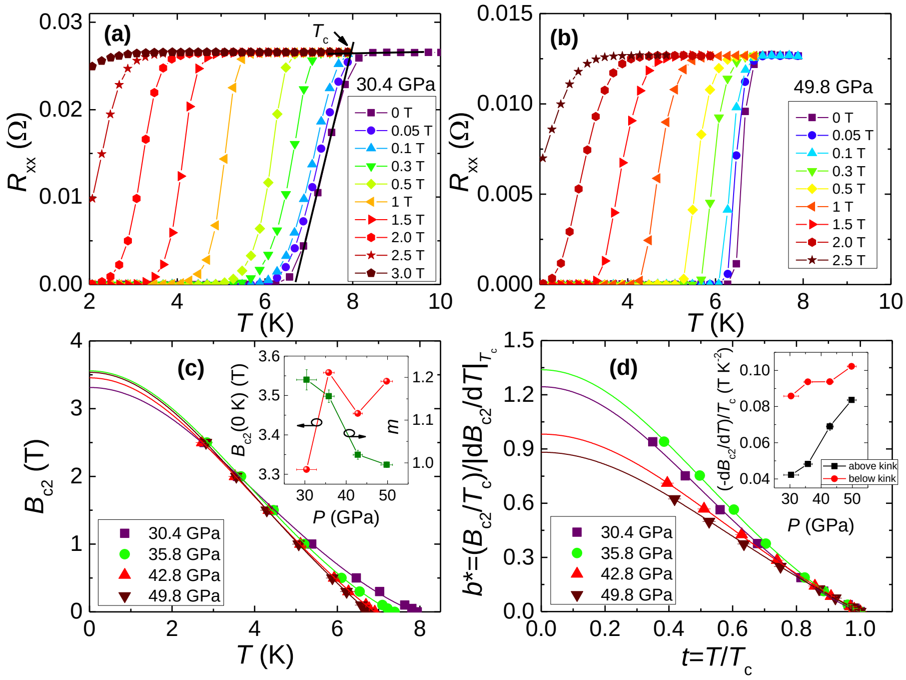

FIG. 5 The $R_{xx}(T)$ under magnetic fields for (a) P=30.4 GPa, (b) P=49.8 GPa. (c) The $B_{c2}(T)$ under various pressures. Inset shows $B_{c2}(P)$ and fitted exponent m. (d). The $b^*(t)$ under various pressures. Solid lines in (c) and (d) are fitted by the modified GL formula.

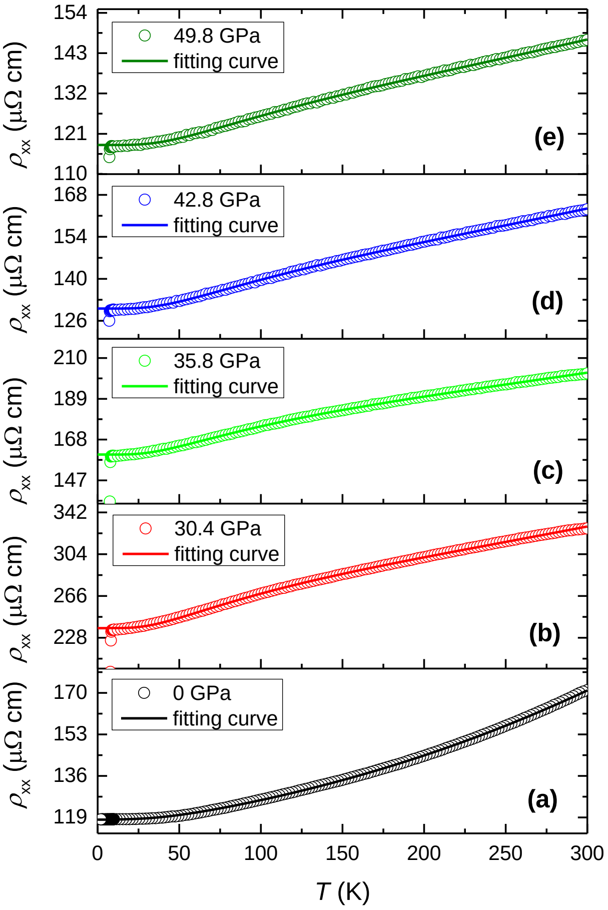

FIG. 6 The temperature dependence of resistivity in bulk $Nb_{0.25}Bi_2Se_3$ at ambient pressure and high pressures.

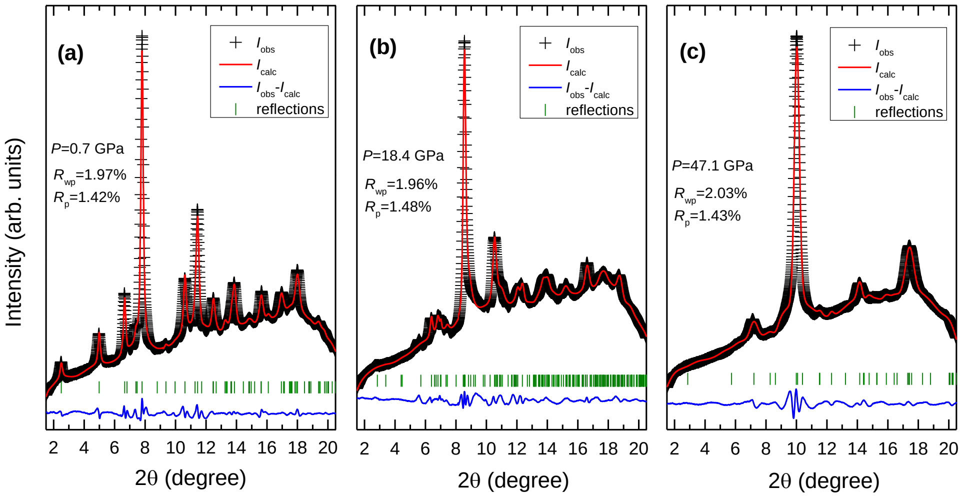

FIG. 7 The representative Rietveld refinement profiles for $Nb_{0.25}Bi_2Se_3$ (a) P=0.7 GPa. (b) P=18.4 GPa. (c) P=47.1 GPa.

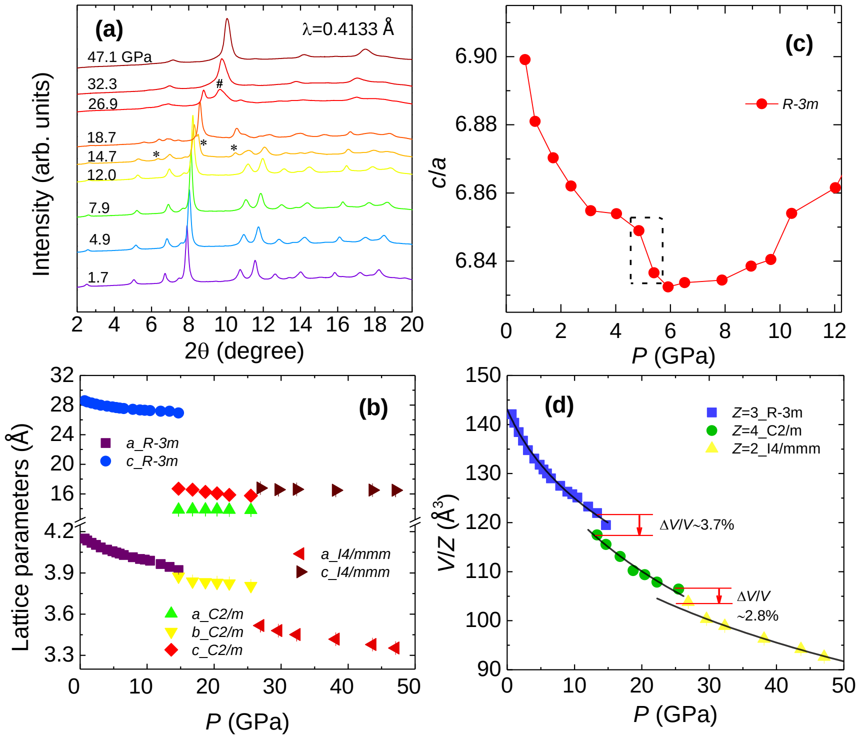

FIG. 8 (a) The selected angle-dispersive XRD patterns under high pressures at room temperature. Symbols of * and # marks the new reflections. (b) The pressure dependence of lattice parameters for the R-phase, the M-phase and T-phase. (c) The ratio of c/a versus pressure for R-phase. (d) The volume per formula unit V/Z versus pressure with the EoS fitting indicated by lines.

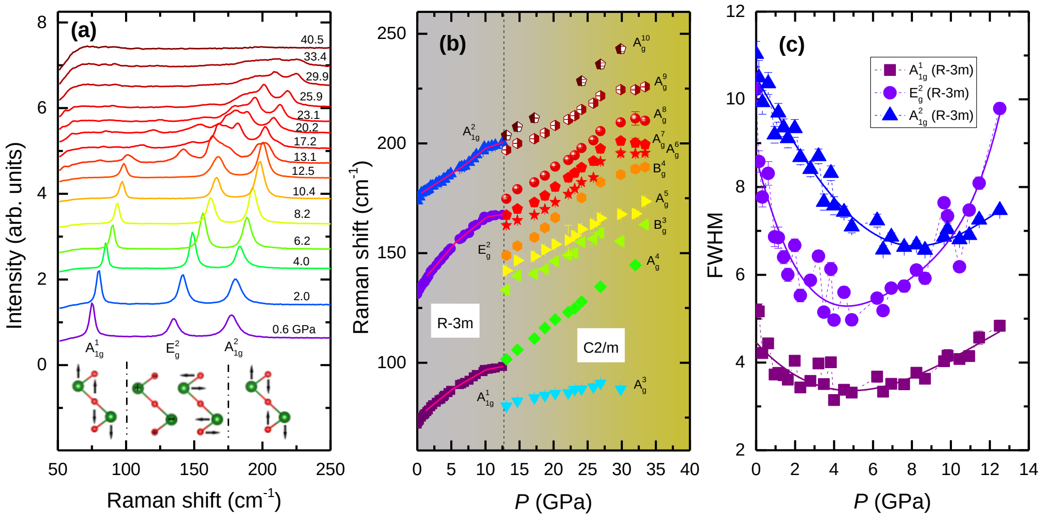

FIG. 9 (a) The selected Raman shift under various pressures at room temperature. The schematic atomic vibration modes for the R-phase were presented at the bottom. The pressure dependence of (b) phonon modes, (e) FWHM in R-phase. The solid lines are guide to eyes.

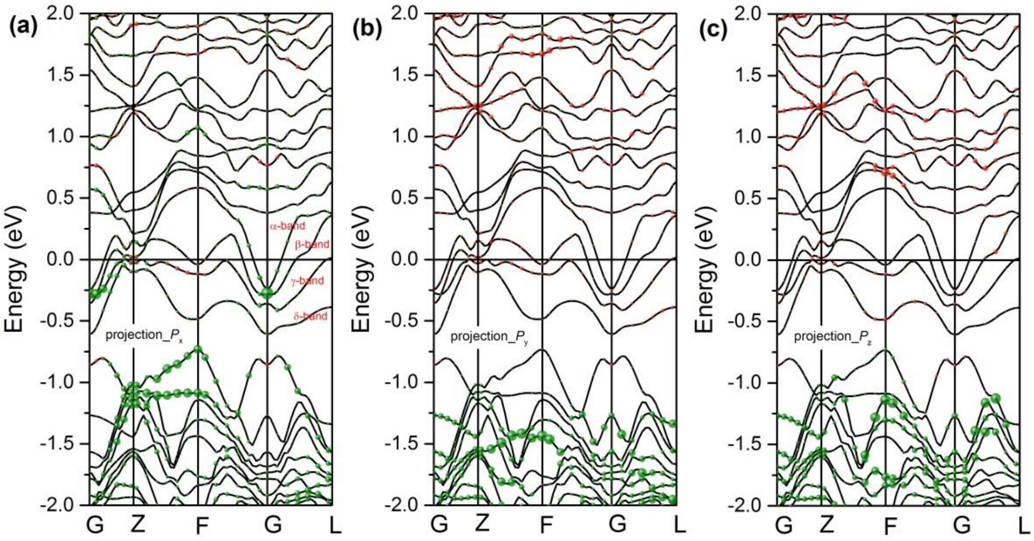

FIG. 10 The band structures for Nb$_{0.25}$Bi$_2$Se$_3$ at 0 GPa. (a) The projection from P_x orbital states, (b) The projection from P_y orbital states, and (c) The projection from P_z orbital states.

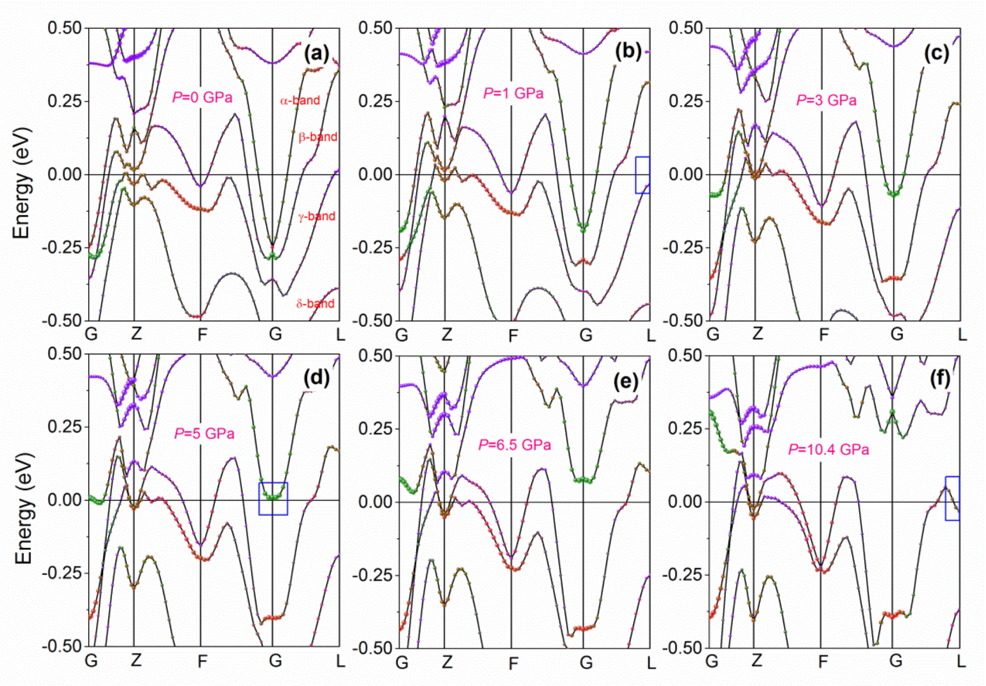

FIG. 11 The band structures of Nb$_{0.25}$Bi$_2$Se$_3$ under different pressures. (a) 0 GPa, (b) 1 GPa, (c) 3 GPa, (d) 5 GPa, (d) 6.5 GPa, and (e) 10.4 GPa. Blue squares indicate the band crossing change at E_F. The violet, red, and green points are projections for the Nb-4d, Bi-6p, and Se-4p orbital states.

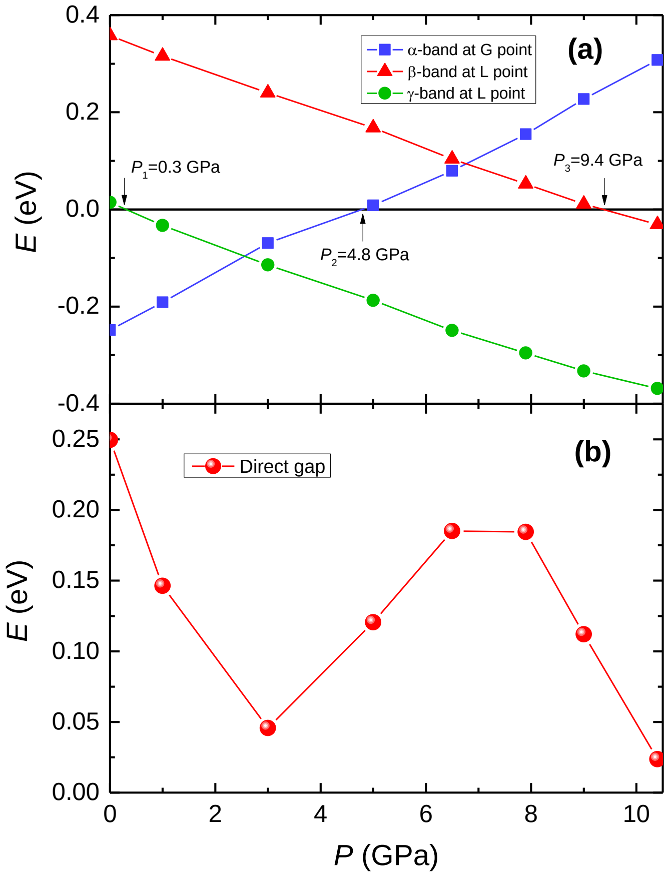

FIG. 12 (a) The pressure dependence of the energy level in the α-band, β-band, and γ-band to the Fermi level at the time reversal invariant point. (b) The pressure dependence of direct band gap at the G point.

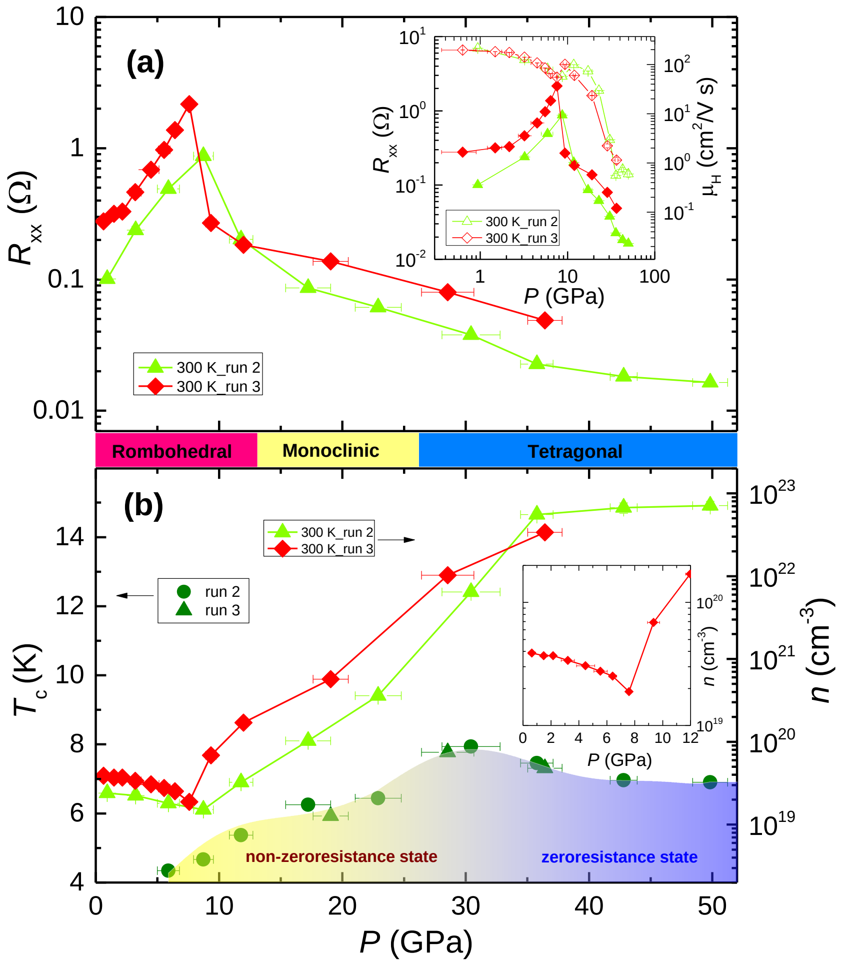

FIG. 13 Phase diagram for $Nb_{0.25}Bi_2Se_3$. (a) $R_{xx}(P)$ at 300 K. (b) $T_c(P)$ and $n(P)$ for runs 2 and 3. The inset of (a) shows the corresponding log-log plot including $\mu_H(P)$. The inset of (b) shows the enlarged view of $n(P)$ at 300 K.

TABLES

TABLE I. The derived physical parameters for T_c, $dB_\mathrm{c2}/dT|_{T_\mathrm{c}}$, $B_\mathrm{c1}(0)$, $B_\mathrm{c}(0)$, γ_s, $N(E_\mathrm{F})$, $B_\mathrm{c2}^\mathrm{orb}(0)$, $B_\mathrm{c2}^\mathrm{GL}(0)$, and $b_\mathrm{GL}^*(0)$ under selected pressures (run 2).

P (GPa)	T_c (K)	$dB_\mathrm{c2}/dT\|_{T_\mathrm{c}}$ (T/K)	$B_\mathrm{c1}(0)$ (mT)	$B_\mathrm{c}(0)$ (mT)	γ_s (mJ/mol K^2)	$N(E_\mathrm{F})$ (states/eV f.u.)	$B_\mathrm{c2}^\mathrm{orb}(0)$ (T)	$B_\mathrm{c2}^\mathrm{GL}(0)$ (T)	$b_\mathrm{GL}^*(0)$	$b_\mathrm{WHH}^*(0)$	$b_\mathrm{pp}^*(0)$
30.4(2.4)	7.94	-0.335(4)	2.68	34.55	1.81	2.02	1.84(2)	3.31(4)	1.24	≅0.693	≅0.85
35.8(1.3)	7.46	-0.360(9)	3.55	40.87	2.80	3.12	1.86(5)	3.56(3)	1.34		
42.8(1.1)	6.96	-0.480(14)	4.13	48.88	4.46	4.97	2.31(7)	3.45(2)	0.98		
49.8(1.4)	6.90	-0.577(9)	4.57	55.82	5.76	6.41	2.76(5)	3.54(2)	0.88		

TABLE II. The fitted and calculated parameters by Eq. (1). The data at 0 GPa is from bulk crystal.

Samples	T_c (K)	P (GPa)	ρ_0 (μΩ cm)	A (μΩ cm/K^2)	B (μΩ cm)	θ (K)	λ
$\mathrm{Bi_2Se_3}$	NA	0	129.26(2)	1.18(0)×10^{-3}	67.02(22)	164.67(38)	NA
$\mathrm{Cu_{0.20}Bi_2Se_3}$	3.54	0	163.82(10)	2.07(4) ×10^{-3}	212.70(4.18)	128.07(1.47)	0.76
$\mathrm{Nb_{0.25}Bi_2Se_3}$	NA	0	118.14(2)	4.95(2)×10^{-4}	13.85(40)	152.10(2.91)	NA
	7.94	30.4	236.79(15)	3.36(6)×10^{-4}	92.56(94)	119.67(1.27)	1.21
	7.46	35.8	160.27(6)	1.36(3)×10^{-4}	45.23(42)	123.26(1.14)	1.13
	6.96	42.8	130.07(5)	1.34(2)×10^{-4}	34.27(42)	142.19(1.49)	0.99
	6.90	49.8	117.93(4)	1.19(2)×10^{-4}	29.53(38)	147.64(1.57)	0.97